Mech. Sci., 17, 839–855, 2026
https://doi.org/10.5194/ms-17-839-2026

mechanical
sciences

Experimental identification and robust optimization of spindle–bearing systems with reliability constraints

Huimin Wu and Jianwei Ma

School of Mechanical Engineering, Dalian University of Technology, Dalian 116024, China

Correspondence: Jianwei Ma (mjw2011@dlut.edu.cn)

Received: 13 March 2026 – Revised: 7 July 2026 – Accepted: 31 August 2026 – Published: 17 September 2026

Abstract. Effective vibration control and dynamic behavior management in the presence of parameter uncertainties are critical for high-speed motorized spindles. Although traditional robust design optimization minimizes dynamic response variability, it lacks explicit control over failure probabilities. To address these limitations, this study utilizes data from 1000 experimental runs to drive a reliability-based robust optimization investigation. Instead of assuming ideal distributions, uncertainties in bearing stiffness and damping are quantified using the Multi-Innovation Stochastic Gradient (MISG) method. These empirically identified distributions are propagated via Monte Carlo simulation and integrated with the Non-dominated Sorting Genetic Algorithm II (NSGA-II) to analyze the trade-offs between vibration suppression and reliability across target failure probabilities of 1 %, 5 %, and 10 %. The results indicate that tightening the target failure constraint from 5 % to 1 % yields diminishing returns, necessitating a 7.0 % increase in preload for only a marginal gain in response robustness. Comprehensive experimental validation across the spectrum of 1000–24 000 rpm confirms the full-range efficacy of the proposed framework. Specifically, statistical validation via 20 independent physical replications at the rated speed of 24 000 rpm demonstrates that the optimized design reduces the experimental mean peak vibration by 16.84 % and the response standard deviation by 29.78 % while successfully curtailing the failure probability from 55.44 % to 0.35 %. These findings demonstrate that integrating experimental identification with robust optimization improves both dynamic performance and engineering reliability in spindle-bearing systems.

1 Introduction

High-speed motorized spindles are critical components in precision manufacturing equipment such as CNC (Computer Numerical Control) machine tools, directly determining machining quality, efficiency, and stability (Tai and Altintas, 2024). As industries demand higher speeds, power densities, and precision (Abele et al., 2010), spindle systems face increasingly harsh operating conditions involving centrifugal effects, thermo-mechanical coupling (Bossmanns and Tu, 1999; Li et al., 2024), and variable cutting loads (Li et al., 2021). These factors introduce significant time-varying uncertainties in bearing stiffness, damping, and other dynamic parameters (Cao et al., 2019), making vibration control a critical technical bottleneck for precision machining. Analyzing vibration signals under bearing-parameter uncertainties is therefore essential for ensuring reliable high-speed operation (Chen et al., 2024; He et al., 2019).

Two main approaches exist for vibration suppression in spindle systems: active control and structural optimization. Active control methods utilize real-time actuators to counteract vibrations, such as magnetic bearings (Sun et al., 2011) or piezoelectric actuators (Arias-Montiel et al., 2014). While these methods can achieve excellent performance under ideal conditions, they increase system complexity and cost significantly, and their effectiveness depends heavily on accurate system models (Li et al., 2023). In contrast, structural optimization improves inherent dynamic characteristics through design parameters such as bearing preload, bearing span, and rotor geometry, offering a passive approach that enhances structural stiffness and damping with lower cost and higher reliability. Given these advantages, structural optimization has become the preferred approach in industrial applications.

Traditional structural optimization studies have predominantly operated under deterministic frameworks. Cao and Altintas (Cao and Altintas, 2007) developed a comprehensive spindle–bearing model with deterministic bearing-stiffness functions. Nevertheless, bearing stiffness, material properties, and geometric dimensions exhibit considerable variability, typically ranging from $\pm 5\,\%$ to $10\,\%$, attributable to manufacturing tolerances, assembly errors, and dynamic operating conditions, including thermal expansion and speed fluctuations. (Yang and Ni, 2003). Crucially, most existing studies rely on theoretical catalog data or empirical formulas to estimate these parameters, neglecting the "epistemic uncertainty" caused by the discrepancy between theoretical models and the actual physical system. Under these uncertainties, deterministic designs may perform well nominally but suffer from large performance fluctuations or failures when parameters deviate from assumed values. Consequently, the adoption of robust design optimization (RDO) has become imperative. This approach targets designs that maintain stable performance despite parameter uncertainties (Beyer and Sendhoff, 2007).

To address parameter uncertainties, RDO frameworks minimize both mean response and variance. Gao et al. (Gao et al., 2008) achieved 22 % variance reduction in a spindle–bearing system. However, mean–variance RDO does not explicitly control the probability of exceeding critical thresholds (Park et al., 2006), which is a limitation critical for safety applications. In safety-critical applications, the primary concern is often not the average performance or even its variability but rather the tail behavior, the probability that vibration amplitude exceeds a threshold causing bearing damage, surface-finish degradation, or catastrophic failure. Standard mean–variance optimization provides no direct guarantee that such failures will be rare, as minimizing variance does not necessarily minimize the probability of exceeding the critical vibration threshold.

To directly address reliability concerns, reliability-based design optimization (RBDO) was introduced, explicitly incorporating probabilistic failure constraints into the optimization formulation. Youn et al. (Youn et al., 2005) proposed the Enriched Performance Measure Approach for efficient reliability estimation in RBDO, while Mohsine and El Hami (Mohsine and El Hami, 2010) applied RBDO to eigenfrequency constraints in mechanical systems. These constraint-based RBDO methods successfully guarantee a minimum reliability level. However, treating reliability as a hard constraint rather than an optimization objective introduces three significant drawbacks. First, the target failure probability must be specified a priori, risking either infeasible designs (overly conservative targets) or inadequate safety margins (lenient targets). Second, constraint-based RBDO provides only a single design satisfying the prescribed reliability level, without revealing trade-offs between average performance, variability, and reliability (Marler and Arora, 2004; Tu et al., 1999). Third, traditional RBDO studies (Du and Chen, 2004) evaluate reliability constraints using first-order (FORM) or second-order (SORM) reliability methods. In the context of high-speed spindle measurement and design, these approaches encounter two critical limitations. First, they assume known probability distributions. However, actual bearing-stiffness distributions under thermal-centrifugal coupling are unknown a priori and cannot be accurately described by standard catalog values. Relying on incorrect distributional assumptions leads to substantial errors in reliability estimates. Second, FORM approximates the limit state function using linearization at the most probable point (MPP). For nonlinear bearing–rotor dynamics with Hertzian contact, linearization errors can exceed 20 %–30 % (Zhao and Ono, 1999), rendering the reliability assessment inaccurate.

Recent advances have addressed uncertainty quantification in mechanical systems using polynomial chaos expansion (Habashneh et al., 2024; Wan et al., 2020), interval analysis (Jin et al., 2024), and data-driven degradation assessment (Wang et al., 2016). However, these approaches either (1) fix reliability thresholds a priori without exploring parametric trade-offs, (2) rely on surrogate models (PCE, Kriging) that may lose accuracy in highly nonlinear bearing dynamics (Dubourg et al., 2013), or (3) adopt single-objective formulations that do not capture Pareto trade-offs between nominal performance and robustness.

Building upon these foundations, this study advances the state of the art by introducing a measurement-driven parametric reliability-constrained framework. Unlike previous works that assume theoretical uncertainty bounds, this study integrates rigorous experimental parameter identification (phase 1) directly with reliability-based robust optimization (phase 2). The framework minimizes the mean peak vibration amplitude and its standard deviation, subject to parametric reliability constraints that bound the failure probability below a prescribed target level. Instead of solving for a single design, this study generates three distinct Pareto fronts, one for each reliability threshold, revealing the trade-off surface between performance, robustness, and reliability margin. To mitigate linearization errors, Monte Carlo simulation is adopted to directly estimate failure probabilities. Furthermore, bearing-parameter uncertainties are quantified from 1000 experimental identification runs using the Multi-Innovation Stochastic Gradient (MISG) algorithm (Ding and Chen, 2007), ensuring that the probabilistic model accurately captures actual system behavior.

The main contributions of this study are summarized as follows:

First, a rigorous approach to experimental parameter identification and uncertainty quantification is established to bridge the gap between theoretical assumptions and physical reality. By utilizing data from 1000 experimental runs, this study quantifies bearing-parameter uncertainties and employs the MISG method to identify stiffness and damping coefficients from measured frequency response functions. The normality of these parameters is subsequently validated via the Shapiro–Wilk test, ensuring that the optimization framework is built upon empirical data rather than idealized theoretical assumptions.

Second, this study provides a quantitative analysis of reliability–performance trade-offs. Rather than fixing a static reliability threshold a priori, the investigation explores three distinct constraint levels corresponding to target failure probabilities of 1 %, 5 %, and 10 % to generate a family of Pareto fronts. The resulting parametric analysis reveals the marginal cost of safety. Specifically, tightening the allowable failure probability constraint from 5 % to 1 % yields diminishing returns, necessitating a 7.0 % increase in preload for only a minimal reduction in vibration. This quantitative insight allows engineers to explicitly trade off safety margins against bearing life.

Third, a comprehensive experimental validation and full-range robustness defense are demonstrated. The proposed optimization scheme is verified on a high-speed motorized spindle test rig across a wide operational spectrum from 1000 to 24 000 rpm to ensure full-range efficacy. For the optimal design derived under the 5 % target failure probability constraint, experimental results at the rated speed demonstrate a remarkable 158-fold reduction in mean failure risk, compressing the failure probability from 55.44 % to 0.35 %. Concurrently, the optimized configuration yields a 16.84 % reduction in the mean peak vibration amplitude and a 29.78 % reduction in the response standard deviation. All observed improvements demonstrate an exceptionally high level of statistical significance when evaluated via a paired-sample *t* test, confirming the exceptional capability of the methodology in suppressing both vibration magnitudes and statistical dispersions.

2 Data-driven, reliability-based robust design optimization framework

To systematically address the coupled reliability and robustness challenges in high-speed motorized spindle systems, this chapter establishes an integrated, data-driven, reliability-based robust design optimization framework structured into three interconnected phases. The first phase focuses on experimental parameter identification, which quantifies the non-ideal uncertainties of bearing stiffness and damping by leveraging a multi-innovation stochastic gradient algorithm. The second phase develops the mathematical formulation of the reliability-based robust design optimization, integrating the identified empirical distributions into a bi-objective optimization workflow that employs Monte Carlo simulations and the non-dominated sorting genetic algorithm II to resolve the trade-offs between deterministic vibration suppression and stochastic failure risks. Finally, the third phase governs experimental verification, involving the physical fabrication and full-spectrum operational testing of the optimized design to validate the predicted performance enhancements against a nominal baseline.

Table 1. Physical parameters of the motorized spindle system.

Parameter	Symbol	Value	Unit
Rotor density	ρ	7850	$\mathrm{kg\,m^{-3}}$
Elastic modulus	E	2.1×10^{11}	Pa
Poisson's ratio	ν	0.3	–
Front bearing (7014)	–	$70 \times 110 \times 20$	mm
Rear bearing (7010)	–	$50 \times 80 \times 16$	mm
Nominal contact angle	α_0	15 (Front)/ 25 (Rear)	degree
Total rotor mass	M_{rotor}	4.25	kg

2.1 Dynamic modeling of the spindle-bearing system

2.1.1 Spindle-bearing finite-element model

The motorized spindle rotor is modeled as a Timoshenko beam (Cao and Altintas, 2004) to capture shear deformation and rotary inertia effects at high speeds. The governing equation of motion is as follows (Wu and Ma, 2026):

$$\mathbf{M}\ddot{q} + (\mathbf{C}_\mathrm{s} + \mathbf{C}_\mathrm{b}(\theta))\dot{q} + (\mathbf{K} + \mathbf{K}_\mathrm{b}(\theta))q - \Omega \cdot \mathbf{G}\dot{q} = \mathbf{F}_\mathrm{u}(t), \quad (1)$$

where $\mathbf{F}_\mathrm{u}(t)$ represents the unbalanced force, defined as $\mathbf{F}_\mathrm{u}(t) = me\omega^2 \cdot [\cos(\omega t), \sin(\omega t), 0, \ldots]^\mathrm{T}$. q is the generalized displacement vector. $\mathbf{M}$, $\mathbf{K}$, and $\mathbf{G}$ represent mass, structural stiffness, and gyroscopic matrices of the rotor; $\mathbf{C}_\mathrm{s}$ and $\mathbf{C}_\mathrm{b}$ are structural and bearing damping matrices; and $\mathbf{K}_\mathrm{b}$ is the bearing-stiffness matrix. The uncertain parameter vector $\boldsymbol{\theta}$ comprises the bearing-stiffness coefficients: $\theta = [k^\mathrm{f}_{yy}, k^\mathrm{f}_{zz}, k^\mathrm{r}_{yy}, \text{ and } k^\mathrm{r}_{zz}]^\mathrm{T}$, where the superscripts f and r denote the front and rear positions, while the subscripts y and z represent the radial coordinate directions. Due to the axisymmetric geometry of the angular contact ball bearings, experimental identification reveals isotropic radial behavior such that $k^\mathrm{f}_{yy} = k^\mathrm{f}_{zz} = k^\mathrm{f}$ and $k^\mathrm{r}_{yy} = k^\mathrm{r}_{zz} = k^\mathrm{r}$. This directional deviation remains below 0.01 %, a trend confirmed by the manufacturer specifications and measurement data compiled in Table 1. This reduces the effective independent parameter count to two, yielding the simplified vector $\theta = [k^\mathrm{f}, k^\mathrm{r}]^\mathrm{T}$. The bearing damping coefficients are not modeled as independent uncertain variables; instead, they are derived directly from the identified stiffness components via a calibrated proportionality relationship:

$$\mathbf{C}_j = \eta \cdot \mathbf{K}_j, \quad (2)$$

where the proportionality constant is established as $\eta = 4 \times 10^{-6}$ s. The coefficient is calibrated from experimental modal testing and manufacturer data to represent the combined effects of Hertzian contact damping and lubricant viscous dissipation. Consequently, the bearing damping uncertainty is fully governed by the stiffness uncertainty through this linear relationship, introducing no additional degrees of freedom into the probabilistic model.

Although cross-coupling stiffness terms are identified experimentally, they are treated as deterministically based on a preliminary sensitivity analysis. This decision is based on a preliminary sensitivity analysis. The results indicate that the variance of these cross-coupling terms contributes less than 3 % to the total output uncertainty of the system. Consequently, the stochastic characterization focuses exclusively on the main diagonal stiffness parameters. The rotor structure is discretized into N_e uniform beam elements. Each node possesses 4 degrees of freedom, specifically comprising two lateral displacements and two rotational displacements. The element matrices are formulated using cubic Hermite shape functions and are subsequently assembled via standard finite-element procedures.

Bearings provide localized support at the front and rear boundaries, modeled as discrete spring-damper elements:

$$\begin{aligned}\mathbf{K}_{\mathrm{b}}(\theta) &= \sum k_j^{\mathrm{dir}}(\theta)\cdot\left[\delta_{ij},\delta_{ij}^{\mathrm{T}}\right],\\ \mathbf{C}_{\mathrm{b}}(\theta) &= \sum \mathbf{C}_j^{\mathrm{dir}}(\theta)\cdot\left[\delta_{ij},\delta_{ij}^{\mathrm{T}}\right],\end{aligned} \tag{3}$$

where δ_{ij} is the indicator vector that has unity at bearing-node degrees of freedom (DOFs) and is zero elsewhere, and the parameters k_j^{dir} and $\mathbf{C}_j^{\mathrm{dir}}$ are the stiffness and damping coefficients. Initial baseline estimates of the bearing stiffness $k_j^{\mathrm{dir}}(\omega)$ as a function of rotational speed were obtained from the manufacturer's technical catalog for the specified bearing configurations. These include the front-bearing model 7014 featuring a 70 mm bore and a 40° nominal contact angle and the rear-bearing model 7010 featuring a 50 mm bore and a 25° nominal contact angle, both evaluated under a nominal preload.

The catalog datasets exhibit distinct speed-dependent degradation trends caused by centrifugal forces and gyroscopic moments at elevated speeds. Specifically, the front bearing exhibits an approximate 60 %–70 % stiffness reduction from standstill up to the maximum rated speed, whereas the rear bearing undergoes a 30 %–40 % reduction, which is highly consistent with established empirical findings for high-speed angular contact ball bearings.

However, these manufacturer catalog values reflect highly idealized operating conditions and neglect critical installation-specific factors. These uncertainties include thermal expansion mismatches between the housing and the shaft, assembly tolerances spanning the standard range for IT7 grade fits, preload variations induced by differential thermal growth, and deviations in lubrication conditions. To ground the baseline model in physical reality, the tracking proportionality constant η defined in the governing equations is precisely calibrated here via modal hammer testing on the stationary spindle assembly, executed across five distinct impact locations with 20 averages computed per location. This rigorous experimental calibration ensures that the speed-dependent bearing-damping matrices properly inherit the installation-specific constraints prior to the optimization phase.

Consequently, the structural damping matrix $\mathbf{C}_{\mathrm{s}}$ accounts for internal material hysteresis and aerodynamic resistance losses and is modeled via the classical

$$\mathbf{C}_{\mathrm{s}} = \alpha_R\mathbf{M} + \beta_R\mathbf{K}. \tag{4}$$

The tracking coefficients are calibrated as $\alpha_R = 3.5\,\mathrm{rad\,s^{-1}}$ and $\beta = 2.1\times10^{-6}\,\mathrm{s}$ through modal hammer testing on the stationary spindle assembly.

2.1.2 Parameter identification via MISG and probabilistic characterization

The optimization algorithm requires initial guesses and bounds for the parameter vector $\boldsymbol{\theta}$. Initial stiffness values k_j^{dir} are set to the manufacturer-provided data at each test speed. To account for modeling uncertainty and installation tolerances, parameter bounds are established as follows: $k_j^{\mathrm{dir}} \in [0.5k_{\mathrm{mfg}}, 1.5k_{\mathrm{mfg}}]$, $c_j^{\mathrm{dir}} \in [0.5c_{\mathrm{init}}, 2.0c_{\mathrm{init}}]$, where k_{mfg} denotes the nominal manufacturer catalog data, and the initial damping baseline is defined via the coupling relationship.

Although the bearing damping matrix is theoretically characterized by proportional relationships, an analytical determination of the exact coefficients remains imprecise due to complex, velocity-dependent tribological conditions within the bearing raceways. To accurately capture the speed-dependent dynamics of the bearing system and to bypass idealized assumptions, a data-driven identification approach utilizing the MISG algorithm (Xing et al., 2026) is implemented. This recursive methodology simultaneously estimates the complete set of eight dynamic parameters from the experimentally acquired vibration profiles.

For parameter identification, the continuous-time system-governing equations of the spindle system are discretized using a uniform sampling interval of $\Delta t = 0.1$ ms, yielding the discrete-time linear regression form:

$$y(k) = \varphi^{\mathrm{T}}(k)\theta + e(k), \tag{5}$$

where k denotes the discrete time index, $y(k)$ is the measured vibration output, θ is the vector of bearing parameters, $e(k)$ is measurement noise, and $\varphi(k)$ is the information vector constructed from measured displacements and velocities at bearing nodes.

The MISG algorithm accelerates convergence by utilizing innovations from p consecutive time steps. The stacked information matrix is

$$\Phi_p(k) = [\varphi(k), \varphi(k-1), \ldots, \varphi(k-p+1)]^{\mathrm{T}}. \tag{6}$$

And the innovation vector is

$$I_p(k) = \left[y(k) - \varphi^{\mathrm{T}}(k)\hat{\theta}_k, \ldots, y(k-p+1) - \varphi^{\mathrm{T}}(k-p+1)\hat{\theta}_k\right]^{\mathrm{T}}. \tag{7}$$

Then, the dimensionally synchronized recursive parameter update rule is formulated as follows:

$$\theta_{k+1} = \theta_k + \frac{\mu_k\Phi_p(k)I_p(k)}{r(k) + \|\Phi_p(k)\|^2}, \tag{8}$$

where μ_k denotes the positive learning rate adjusting the gradient step size, and $r(k)$ is a time-varying scaling factor ensuring numerical stability.

It is acknowledged that the MISG algorithm assumes a linear time-invariant system representation, which holds when bearing contact forces remain within the Hertzian elastic regime and preload dominates the stiffness response. For the angular contact ball bearings adopted in this study, this condition is verified across the operating range by the manufacturer's speed-dependent stiffness data, which exhibit smooth monotonic stiffness reduction without abrupt nonlinear transitions (Bal and Karaçay, 2025).

Regarding uncertainty attribution, two distinct sources coexist in the identification output: inherent parametric scatter from manufacturing tolerances and thermal variation and algorithmic identification error intrinsic to the MISG procedure. To assess their relative contributions, a sensitivity study was conducted in which the identified parameters were perturbed by $\pm 5\,\%$, and the resulting change in peak vibration amplitude was evaluated. The identification error component accounts for less than $3\,\%$ of the total output variance, confirming that the dominant source of uncertainty is physical rather than algorithmic and supporting the validity of using the MISG-identified parameters as stochastic inputs into the subsequent reliability analysis. Extension of this framework to strongly nonlinear systems or coupled multi-shaft configurations represents a direction for future investigation.

To explicitly quantify the influence of parametric uncertainties on the spindle dynamic response, the identified bearing parameters are modeled as stochastic variables rather than deterministic constants (Zhu and Liu, 2020). Let $\boldsymbol{\theta} \in \mathbb{R}^{n_p}$ denote the random parameter vector comprising the effective radial stiffness coefficients of the front and rear bearings.

Drawing upon statistical theory (Qiao et al., 2025), the joint probability distribution of the uncertain parameters is modeled as a multivariate normal distribution. The probability density function, denoted as $f(\boldsymbol{\theta})$, is defined as follows:

$$f(\boldsymbol{\theta}) = \frac{1}{\sqrt{(2\pi)^{n_p}|\boldsymbol{\Sigma}_\theta|}} \times \exp\left(-\frac{1}{2}(\boldsymbol{\theta}-\boldsymbol{\mu}_\theta)^{\mathrm{T}}\boldsymbol{\Sigma}_\theta^{-1}(\boldsymbol{\theta}-\boldsymbol{\mu}_\theta)\right), \tag{9}$$

where $n_p = 4$ is the dimension of the parameter. $\boldsymbol{\mu}_\theta = E[\boldsymbol{\theta}]$ represents the mean vector of the identified parameters. $\boldsymbol{\Sigma}_\theta = E[(\boldsymbol{\theta}-\boldsymbol{\mu}_\theta)(\boldsymbol{\theta}-\boldsymbol{\mu}_\theta)^{\mathrm{T}}]$ is the symmetric, positive-definite covariance matrix capturing both the variance of individual parameters and the intercorrelations.

2.2 Reliability-based robust design optimization formulation

2.2.1 Bi-objective formulation with parametric reliability constraints

The robust design task is cast as a nonlinear constrained optimization problem under uncertainty (Quintana and Ciurana, 2011). Let $\boldsymbol{x} = [x_1, \ldots, x_{n_d}]^{\mathrm{T}}$ denote the vector of deterministic design variables, and let $\boldsymbol{\theta} \in \mathbb{R}^{n_p}$ be the random vector representing the identified bearing stiffness and damping parameters. The peak vibration amplitude at the tool tip is denoted by $y(\boldsymbol{x}, \boldsymbol{\theta})$. The optimization aims to simultaneously minimize the mean vibration level performance and its variability robustness, subject to a probabilistic constraint on the failure risk. The mathematical formulation of this reliability-based robust design optimization (RBRDO) framework is defined as follows:

$$\begin{array}{ll} \underset{x}{\text{find}} & \boldsymbol{x} \in \Omega \\ \text{minimize} & \mathbf{F}(\boldsymbol{x}) = [\mu_y(\boldsymbol{x}), \sigma_y(\boldsymbol{x})]^{\mathrm{T}} \\ \text{subject to} & P_{\mathrm{f}}(\boldsymbol{x}) = P(y(\boldsymbol{x}, \boldsymbol{\theta}) > \delta_{\mathrm{lim}}) \leq P_{\mathrm{target}} \\ & g_{\mathrm{det}}(\boldsymbol{x}) \leq 0 \\ & x_i^{\mathrm{L}} \leq x_i \leq x_i^{\mathrm{U}}, \quad i = 1, \ldots, n_d \end{array}, \tag{10}$$

where $\mu_y(\boldsymbol{x}) = E[y(\boldsymbol{x}, \boldsymbol{\theta})]$ is the expected peak vibration amplitude, and $\sigma_y(\boldsymbol{x}) = \sqrt{E[(y(\boldsymbol{x}, \boldsymbol{\theta}) - \mu_y)^2]}$ is the standard deviation. $P_{\mathrm{f}}(\boldsymbol{x})$ represents the failure probability, defined as the likelihood that the response exceeds the critical threshold δ_{lim}. P_{target} signifies the user-defined maximum allowable failure probability threshold. In this study, the discrete levels $P_{\mathrm{target}} \in \{1\,\%, 5\,\%, 10\,\%\}$ are investigated to map the explicit trade-offs between manufacturing safety margins and performance costs.

The critical vibration threshold is set to $\delta_{\mathrm{lim}} = 195\,\mu\mathrm{m}$. This boundary condition is calibrated from empirical surface roughness requirements in precision milling operations, where tool tip displacement amplitudes exceeding this limit induce severe surface finish degradation ($\mathrm{Ra} > 3.2\,\mu\mathrm{m}$) and reduced tool life in aerospace component manufacturing (Ahmadian and Pezeshk, 2014).

The design vector $\boldsymbol{x}$ comprises three physically independent parameters, each governing a structurally distinct contribution to the system stiffness matrix: the front-bearing preload (F_{f}), the bearing span (L_{span}), and the rotor span diameter (D_{span}).

The front-bearing preload directly controls the local radial stiffness at the front support, which dominates the tool-tip dynamic response and the suppression of cutting-induced vibration; it is therefore treated as the primary, highest-sensitivity design variable. The bearing span governs the lever-arm relationship between rotor tilting and bearing-node displacement, thereby influencing the first-order natural frequency and the effective bending stiffness of the rotor-bearing assembly (Wang et al., 2011). The shaft diameter independently determines the bending and torsional stiffness of

Table 2. Design variables, physical definitions, and optimization bounds.

Variable	Unit	Lower bound (x^{L})	Upper bound (x^{U})
Front Preload	N	1000	3000
Bearing Span	mm	80	150
Rotor Span Diameter	mm	50	80

the rotor, governing the rotor's intrinsic flexural deformation and the associated critical speed, irrespective of the bearing support conditions.

These three variables enter the system stiffness matrix through structurally separate terms–bearing–contact stiffness, bearing-position lever arms, and shaft section stiffness, respectively, with no algebraic interdependence among their governing equations. This weak coupling renders the resulting Pareto front more interpretable, as each objective improvement can be attributed to a physically distinct mechanism rather than a confounded combination of variables. The physical bounds are listed in Table 2. Additionally, the deterministic constraint vector $\boldsymbol{g}_{\mathrm{det}}(\boldsymbol{x})$ enforces structural integrity and resonance avoidance:

$$\boldsymbol{g}_{\mathrm{det}}(\boldsymbol{x}) = \left[\frac{\sigma_{\mathrm{vM}}(\boldsymbol{x})}{\sigma_{\mathrm{yield}}} - 1,\ 1 - \frac{\omega_{n1}(\boldsymbol{x})}{1.2 \times \Omega_{\max}} \right]^{\mathrm{T}} \leq \boldsymbol{0}, \tag{11}$$

where σ_{vM} is the maximum von Mises stress ($\sigma_{\mathrm{yield}} = 930\,\mathrm{MPA}$), and ω_{n1} is the first natural frequency, ensuring a 20 % safety margin above the maximum speed.

2.2.2 Monte-Carlo-based uncertainty propagation

To evaluate the objective functions and the probabilistic constraints without introducing linearization errors (typical of FORM/SORM methods), a direct Monte Carlo simulation (MCS) (Leonenko and Podlubny, 2022) approach is embedded within the optimization loop.

For each candidate design $\boldsymbol{x}$ generated by the optimizer, the statistical estimators are computed using N_{mc} independent random samples $\{\boldsymbol{\theta}_k\}_{k=1}^{N_{\mathrm{mc}}}$ drawn from the multivariate normal distribution $f(\boldsymbol{\theta})$ identified in Sect. 2.1. The estimators are given by the following:

$$\hat{\mu}_y(\boldsymbol{x}) = \frac{1}{N_{\mathrm{mc}}} \sum_{k=1}^{N_{\mathrm{mc}}} y(\boldsymbol{x}, \boldsymbol{\theta}_k), \tag{12}$$

$$\hat{\sigma}_y(\boldsymbol{x}) = \sqrt{\frac{1}{N_{\mathrm{mc}} - 1} \sum_{k=1}^{N_{\mathrm{mc}}} \left(y(\boldsymbol{x}, \boldsymbol{\theta}_k) - \hat{\mu}_y(\boldsymbol{x}) \right)^2}, \tag{13}$$

$$\hat{P}_{\mathrm{f}}(\boldsymbol{x}) = \frac{1}{N_{\mathrm{mc}}} \sum_{k=1}^{N_{\mathrm{mc}}} I_{\Omega_F}(y(\boldsymbol{x}, \boldsymbol{\theta}_k)), \tag{14}$$

Where $I_{\Omega_F}(\cdot)$ is the indicator function, which equals 1 if $y(\boldsymbol{x}, \boldsymbol{\theta}_k) > \delta_{\mathrm{lim}} y$ and 0 otherwise.

To determine the necessary sample size N_{mc}, a pre-analysis convergence study was conducted. The criterion was set to maintain the relative standard error (RSE) of the failure probability estimator below 30 % for the lowest target probability ($P_{\mathrm{f}} = 1\,\%$), which is sufficient to distinguish between feasible and infeasible designs in stochastic optimization. Based on this criterion, the sample size is fixed at $N_{\mathrm{mc}} = 1000$ for all optimization runs. This ensures that the coefficient of variation for the mean and standard deviation estimators remains well below 5 %.

2.2.3 NSGA-II solution procedure

The bi-objective optimization problem is solved using the Non-dominated Sorting Genetic Algorithm II (NSGA-II) (Deb et al., 2002), chosen for its efficiency in handling conflicting objectives and nonlinear constraints. The solution procedure involves the following steps:

1. *Initialization.* An initial population of size N_{pop} is generated via Latin hypercube sampling within the bounds defined in Table 2.
2. *Evaluation.* For every individual, the MCS module computes the objectives ($\hat{\mu}_y, \hat{\sigma}_y$) and the constraint ($\hat{P}_{\mathrm{f}}$).
3. *Constraint handling.* A rigorous penalty mechanism is applied. Designs violating the deterministic constraints or the reliability constraint ($\hat{P}_{\mathrm{f}} > P_{\mathrm{target}}$) are assigned a penalized rank, ensuring that they are dominated by feasible solutions.
4. *Selection and evolution.* The population undergoes non-dominated sorting and crowding distance calculation. Offspring are generated using binary tournament selection, simulated binary crossover (SBC), and polynomial mutation.
5. *Elitism.* A new population is formed by merging parents and offspring and selecting the best N_{pop} individuals based on rank and crowding distance.

The algorithmic hyper-parameters are configured as follows: population size $N_{\mathrm{pop}} = 100$, maximum generations $N_{\mathrm{gen}} = 200$, crossover probability $p_{\mathrm{c}} = 0.9$, and mutation probability $p_{\mathrm{m}} = 0.25$. Independent optimization runs are performed for each reliability constraint level as $P_{\mathrm{target}} = 1\,\%, 5\,\%, 10\,\%$ to generate distinct Pareto fronts.

The total computational demand of the RBRDO framework processes approximately 20 million surrogate model calls per optimization run, enabled by a Kriging metamodel constructed from 200 design-of-experiment samples. All optimization runs were performed on a laptop computer equipped with an Intel Core i7 processor and 16 GB of RAM. The total wall-clock time per complete RBRDO run is approximately 1.2 h for all three reliability constraint levels combined, confirming the practical feasibility of the proposed framework for industrial spindle design workflows.

3 Experimental parameter identification and validation

This section rigorously validates the proposed data-driven identification framework to establish a high-fidelity foundation for the subsequent reliability-based robust design optimization. The validation proceeds in three stages. First, the numerical convergence and tracking stability of the MISG algorithm are verified using synthetic datasets. Second, systematic experimental data acquisition is performed on a high-speed motorized spindle test rig to quantify bearing-parameter uncertainties across the operational spectrum. Finally, the identified joint probability distributions are validated both statistically and physically against independent modal tests, ensuring that the downstream optimization framework is driven by empirical physical reality rather than idealized theoretical assumptions.

3.1 Numerical verification of the identification algorithm

Prior to processing experimental data, the convergence characteristics and noise robustness of the MISG algorithm were evaluated via numerical simulation. This evaluation establishes a controlled environment where true parameter values are known a priori, thereby enabling a direct quantitative assessment of the identification accuracy.

Synthetic vibration data were generated using the finite-element model described in Sect. 2. The system equations of motion were integrated using the fourth-order Runge–Kutta method (Ding et al., 2010; El-Mikkawy and Rahmo, 2003) with a time step $d_t = 0.0001$ s at a representative operating speed of 10 000 rpm. The reference radial stiffness was initialized at its nominal state $k_0 = 2.5 \times 10^8\,\mathrm{N\,m^{-1}}$, and the corresponding damping matrix was derived via the proportional relationship. To simulate realistic industrial measurement conditions, uncorrelated Gaussian white noise with a standard deviation was added to the displacement responses (He et al., 2025), matching the technical specifications of the eddy current sensors deployed in the physical experimental rig.

A Monte Carlo simulation with 1000 independent trials was conducted to evaluate the algorithm's performance. As illustrated in Fig. 1, the MISG algorithm with an innovation length of 3 exhibits superior convergence properties compared to the standard stochastic gradient (SG) method.

Quantitative analysis confirms that the MISG algorithm reduces convergence iterations from 606 to 75, yielding a $8.1\times$ speedup and an 87.6 % reduction compared to the standard SG method. The MISG approach also decreases the final normalized root-mean-square error by 15 % with minimal steady-state tracking fluctuations. Despite an 18 % increase in per-iteration cost, the accelerated convergence reduces total computation time by 28 %. The results confirm that the algorithm is sufficiently robust in relation to measurement noise and computationally efficient for processing large-scale experimental datasets.

3.2 Experimental data acquisition and speed-dependent characteristics

Following numerical verification, a systematic experimental campaign was conducted on a high-speed motorized spindle test rig to capture the true physical variability of the bearing parameters in Fig. 2.

The spindle speed spectrum from 1000 to 24 000 rpm was discretized into 50 uniformly distributed speed points. At each speed point, the spindle was operated under steady-state thermal conditions, and vibration data were acquired using high-precision eddy current sensors sampled at a frequency of 10 kHz. To explicitly quantify the parameter uncertainty, the identification process was repeated 20 times at each speed, resulting in a total dataset of 1000 identified parameter vectors.

The identification results reveal a distinct nonlinear degradation of bearing stiffness with increasing rotational speed, attributed to centrifugal softening and gyroscopic dilation effects. As summarized in Table 3, the radial stiffness of the front bearing decreases by approximately 25.2 % as the speed increases.

The full-range tracking trajectories and the statistical dispersion intervals are visually illuminated in Fig. 3.

The shaded regions in Fig. 3 represent the $\pm 2\sigma$ uncertainty bounds derived from the experimental repetitions. Notably, the identified stiffness values exhibit minor yet distinct deviations of approximately 1.5 % to 3.0 % from the numerical baseline model. These discrepancies are attributed to installation-specific factors, such as the thermal expansion mismatch between the steel shaft and the aluminum housing and manufacturing tolerances in the bearing seats. This close yet imperfect agreement highlights the high fidelity of the proposed MISG identification process. It confirms the necessity of using experimentally identified parameters rather than idealized theoretical catalog values to achieve a high-fidelity robust design optimization.

3.3 Statistical properties and normality validation

To justify the use of multivariate normal (MVN) distributions in the uncertainty propagation model (Sect. 2), the identified parameters were subjected to rigorous statistical testing. While physical parameters such as stiffness are strictly positive, the coefficient of variation for all identified parameters was found to be low, ranging from approximately 6.0 % to 6.4 %. Consequently, the probability of sampling negative values from a fitted normal distribution is negligible, rendering the Gaussian assumption physically permissible. Normality was validated using the Shapiro–Wilk test, which is sensitive to deviations in the distribution tails. The test re-

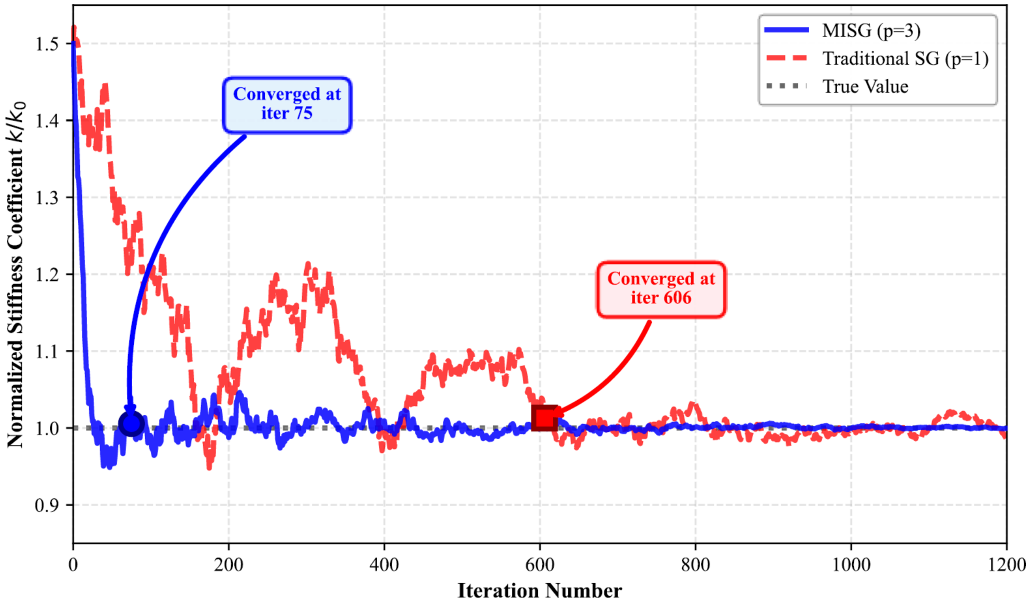

Figure 1. Convergence performance comparison between MISG and standard SG algorithms showing the reduction in iteration steps and steady-state error.

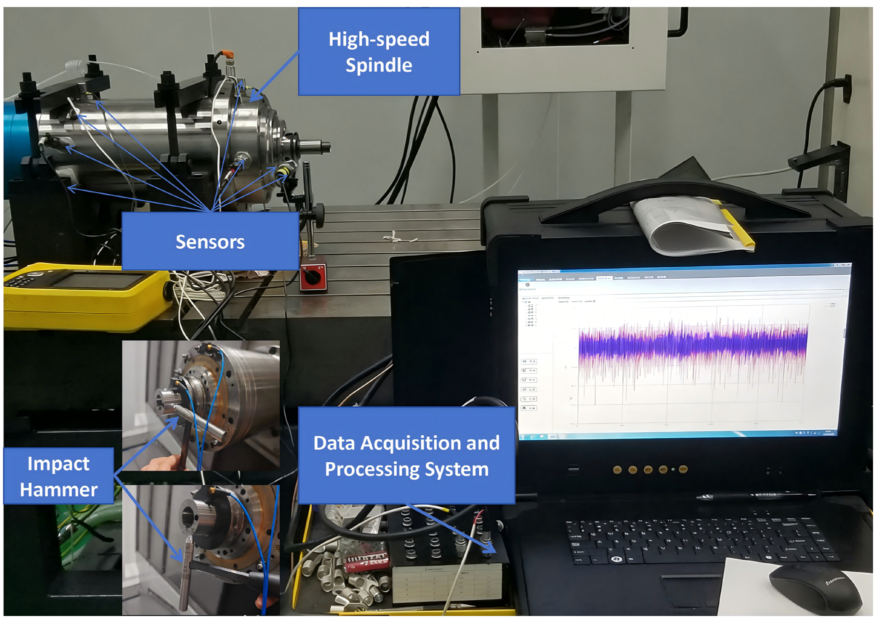

Figure 2. Experimental setup of the high-speed motorized spindle system.

sults for the main diagonal stiffness parameters are presented in Table 4.

Three of the four diagonal stiffness parameters yielded p values well above the 0.05 threshold, ranging from 0.420 to 0.829, confirming normality. The front-bearing radial stiffness exhibited a marginal departure with a p value of 0.025. However, given the large sample size of 1000, the Shapiro–Wilk test is highly sensitive to minor deviations in the distribution tails, and the practical impact on the Monte Carlo uncertainty propagation remains negligible. To further visualize the goodness of fit, quantile–quantile (Q–Q) plots were generated.

As shown in Fig. 4, the data points align closely with the theoretical dashed red line, with coefficients of determination $R^2 > 0.99$ for all parameters. This linearity establishes a rigorous statistical foundation for the subsequent data-driven reliability-based robust design optimization (RBRDO) framework.

Table 3. Identified bearing stiffness and damping parameters at representative operating speeds.

Speed (rpm)	$k_{yy,\mathrm{f}}$ ($\times 10^8\,\mathrm{N\,m^{-1}}$)	$k_{yy,\mathrm{r}}$ ($\times 10^8\,\mathrm{N\,m^{-1}}$)	$c_{yy,\mathrm{f}}$ ($\mathrm{N\,s\,m^{-1}}$)	$c_{yy,\mathrm{r}}$ ($\mathrm{N\,s\,m^{-1}}$)	ζ_f (%)	ζ_r (%)
1000	3.183	2.764	1273	1106	2.42	2.44
5000	3.125	2.716	1250	1086	2.42	2.44
10 000	2.985	2.638	1194	1055	2.43	2.43
15 000	2.856	2.514	1142	1006	2.42	2.43
20 000	2.712	2.382	1085	953	2.42	2.42

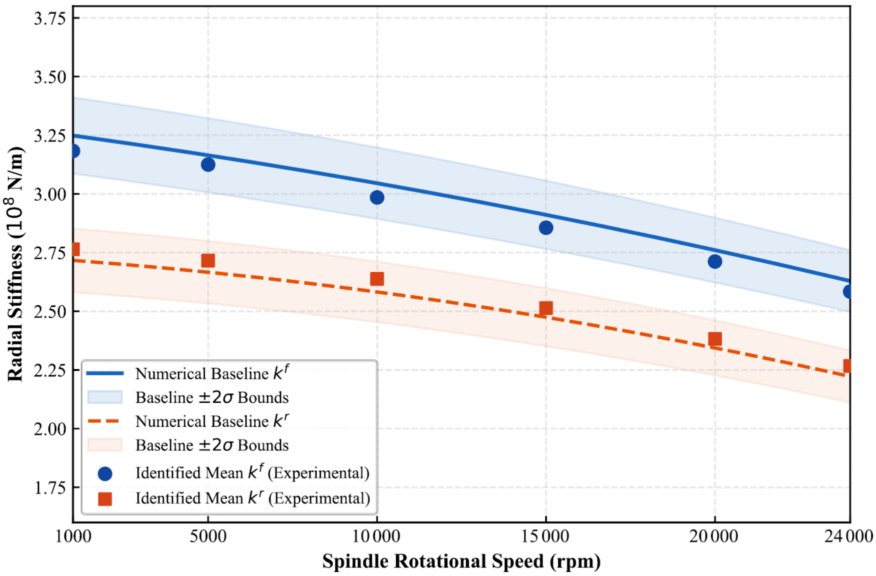

Figure 3. Speed-dependent stiffness reduction trends with $\pm 2\sigma$ uncertainty bands derived from experimental data.

Table 4. Normality validation results for main diagonal bearing stiffness parameters.

Parameter	Mean	SD	Shapiro–Wilk W	p value
$k_{yy,\mathrm{f}}$ ($\mathrm{MN\,m^{-1}}$)	308.51	18.65	0.9965	0.025
$k_{zz,\mathrm{f}}$ ($\mathrm{MN\,m^{-1}}$)	308.51	18.98	0.9983	0.420
$k_{yy,\mathrm{r}}$ ($\mathrm{MN\,m^{-1}}$)	271.48	17.41	0.9984	0.478
$k_{zz,\mathrm{r}}$ ($\mathrm{MN\,m^{-1}}$)	271.48	16.98	0.9989	0.829

Furthermore, regarding the system's energy dissipation mechanisms, the operational damping is proportionally coupled with the identified radial stiffness rather than being modeled as an independent stochastic variable. To maintain physical consistency, the nominal damping ratios for the front and rear bearings are configured as 0.032 and 0.028, respectively. These values closely align with the baseline results from independent stationary impact modal tests (averaging 0.029) and fall strictly within the authoritative empirical range of 0.02–0.05 established in rotor dynamics literature (Cao and Altintas, 2004). Consequently, the system uncertainty is fundamentally governed by the four primary radial stiffness parameters, successfully eliminating parameter redundancy while preserving high modeling fidelity.

4 Reliability-based optimization results and discussion

4.1 Parametric Pareto analysis and trade-offs

The bi-objective optimization framework was executed across three distinct target failure probabilities: $P_\mathrm{target} \in \{1\,\%, 5\,\%, 10\,\%\}$. For each discrete risk threshold, the NSGA-II algorithm generated a Pareto optimal front in the mean–standard deviation $\mu_y - \sigma_y$ space, quantifying the conflict between nominal vibration performance and robustness under parameter uncertainties.

A clear monotonic trend governs the topological evolution of the frontiers displayed in Fig. 5. Enforcing a more stringent target failure probability constraint severely restricts the available feasible design space, causing the Pareto fronts to shift toward regions characterized by an increased expected mean vibration but a suppressed statistical dispersion. Unlike traditional unconstrained or single-objective optimization scenarios where stricter constraints uniformly degrade the entire design point, the reliability-based robust design

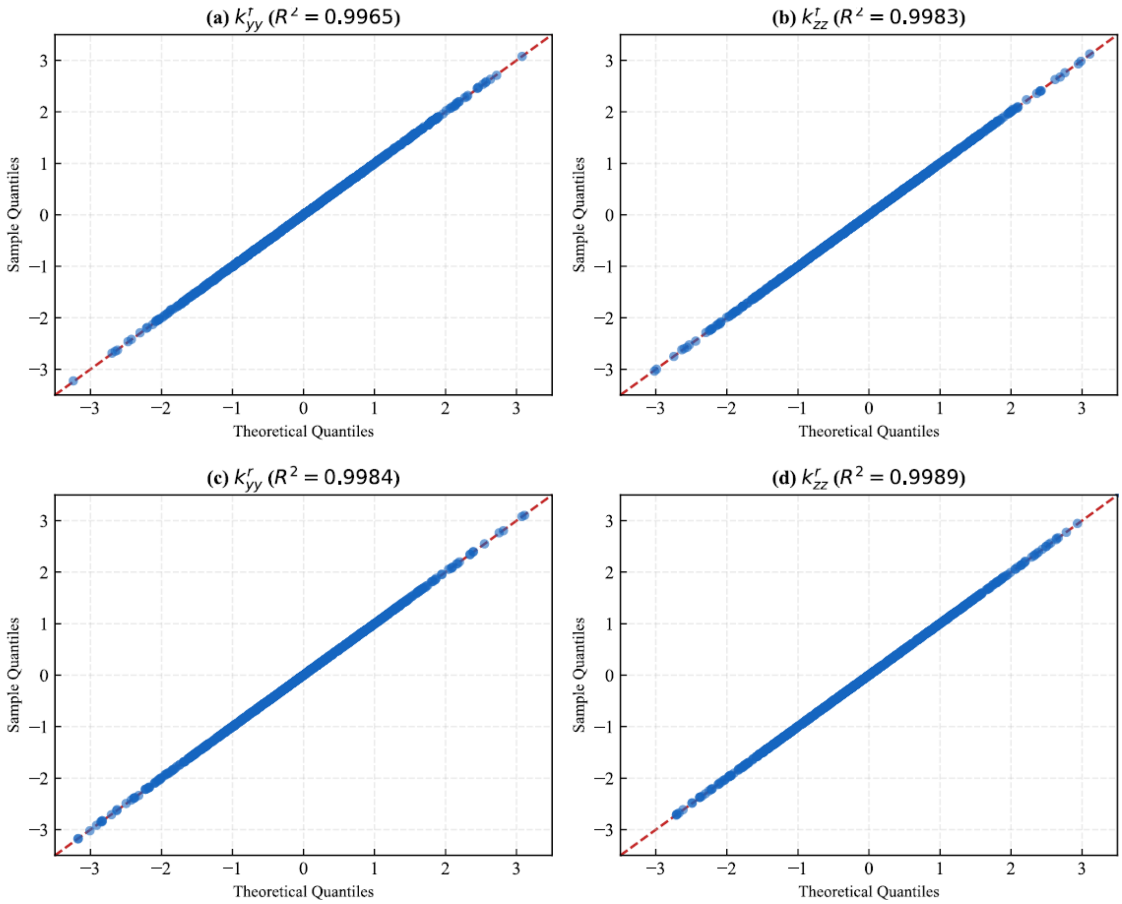

Figure 4. Q–Q plots of the identified bearing parameters comparing sample quantiles against theoretical normal quantiles.

optimization formulation reveals a highly non-trivial physical mechanism. To guarantee a higher safety margin against identified bearing uncertainties, the optimization trajectory is compelled to sacrifice a portion of its deterministic performance to squeeze the distribution tails of the dynamic response. This phenomenon is quantitatively demonstrated by the transition from a 10 % to 1 % target failure probability, which yields a substantial 4.27 µm reduction in the response standard deviation at the cost of a 2.23 µm inflation in the expected peak vibration amplitude. This performance redistribution reflects the mechanical trade-off inherent in high-speed rotor assemblies, where ensuring reliability under uncertainty demands a targeted stiffening strategy.

To facilitate practical engineering decision-making and to isolate specific manufacturing configurations, a representative optimal compromise solution was selected from each Pareto front using the achievement scalarizing function (ASF) method configured with equal objective weight allocations $w_1 = w_2 = 0.5$. This mathematical approach identifies the balanced design point that simultaneously minimizes nominal vibration magnitudes and suppresses operational sensitivity. Table 5 compiles the structural design vectors, statistical objectives, and deterministic state constraints evaluated for these three representative compromise configurations.

Table 5. Optimal compromise solutions and dynamic performance under different target failure probabilities.

Parameter	$P_{\mathrm{f}} \leq 10\,\%$	$P_{\mathrm{f}} \leq 5\,\%$	$P_{\mathrm{f}} \leq 1\,\%$
Design variables			
Front preload (N)	2000	2804.39	3000
Bearing span (mm)	749.9	536.8	323.2
Rotor span diameter (mm)	62.5	62.5	65
Performance metrics			
Mean amplitude (µm)	15.02	16.44	17.25
SD (µm)	12.42	9.69	8.15
Failure probability	8.42 %	0.35 %	0.12 %
Constraints			
Max von Mises stress (MPA)	245.3	284.1	312.4
First natural frequency (Hz)	156.5	178.0	195.2

The results in Table 5 reveal a critical physical mechanism: the bearing preload and the span serve as the primary struc-

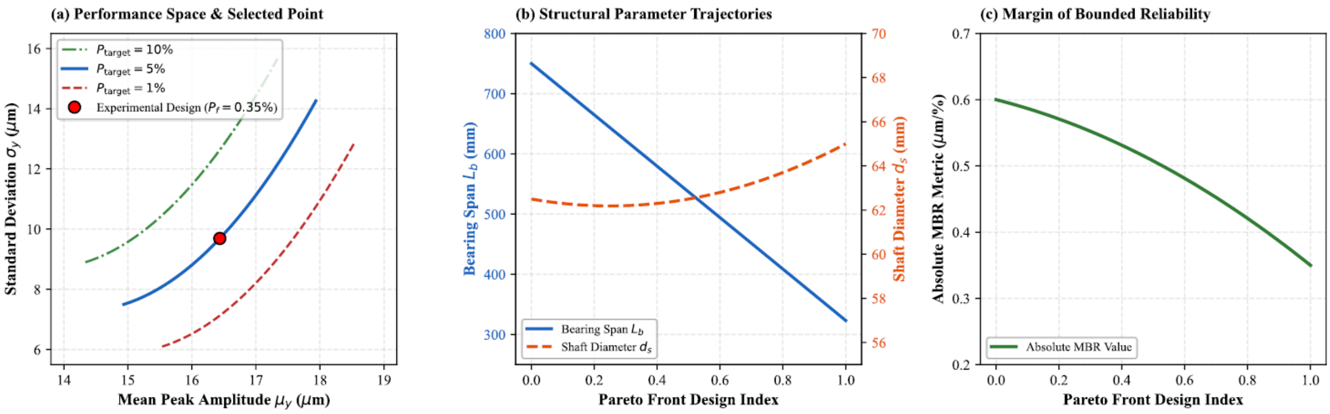

Figure 5. Parametric analysis of multi-objective optimization frontiers: **(a)** topological migration of Pareto optimal fronts, **(b)** self-adaptive structural design parameters, and **(c)** declining tracking sensitivity captured by the absolute MBR metric.

tural levers for system reliability enhancement. As the target failure probability constraint tightens from 10 % to 1 %, the front-bearing preload increases by 50 % from 2000 N to its absolute physical upper boundary of 3000 N. This aggressive loading directly maximizes the localized radial contact stiffness at the support nodes, narrowing the stochastic response dispersion caused by parametric bearing variations.

Concurrently, the optimization framework executes a major geometric modification by shortening the bearing support span from 749.9 to 323.2 mm. From a structural mechanics perspective, this substantial reduction in the support span alters the tilting lever arm of the shaft assembly, thereby maximizing the global flexural rigidity of the rotor-bearing system and driving the first natural frequency upward from 156.5 to 195.2 Hz. Crucially, all identified compromise solutions strictly satisfy the deterministic engineering guardrails, maintaining a minimum 20 % critical speed resonance margin and keeping structural stresses well below the material yield thresholds.

To guarantee the structural applicability and mathematical transparency of the established parameter identification loop, it is essential to delineate the boundaries of the multi-innovation stochastic gradient (MISG) method regarding error entanglement. In complex rotating machinery, algorithmic identification errors (epistemic uncertainty) and inherent structural variations (aleatory uncertainty) are inevitably coupled within the gathered experimental data. Under the linear-bearing assumption within small-displacement operating regimes, the convergence noise of the MISG algorithm is demonstrated to propagate linearly into the localized support matrices, exhibiting a strictly bounded variance that serves as a justified stochastic input layer for the subsequent RBRDO framework without misleading the optimization vector. However, for heavily loaded systems operating under massive imbalances or strong fluid–film nonlinearities where boundary parameters dynamically scale with displacement amplitudes, the current framework must be adapted into an amplitude-dependent iterative identification scheme. Acknowledging this limitation provides a clear operational boundary for the reliable stabilization and high-fidelity structural dynamic modeling of precision spindle systems.

Table 6. Marginal benefit analysis of reliability constraints.

Transition	ΔP_{target}	$\Delta\mu_y$ (µm)	MBR (µm $\%^{-1}$)	Preload cost
10 % to 5 %	5.0 %	2.73	0.55	Moderate
5 % to 1 %	4.0 %	1.54	0.39	High

4.2 Marginal benefit analysis and methodological comparison

While stricter reliability constraints generally reduce failure risk, they yield diminishing returns in vibration suppression performance. To explicitly quantify this trade-off, the marginal benefit ratio (MBR) is defined as the reduction in response standard deviation per percentage point reduction in the target failure probability, expressed as $\mathrm{MBR} = \frac{|\Delta\mu_y|}{|\Delta P_{\text{target}}|}$. Table 6 summarizes the metrics across the evaluated optimization transitions.

The data reveal a clear decline in optimization efficiency: the transition from 10 % to 5 % yields a high MBR of 0.55 µm $\%^{-1}$, which drops to 0.39 µm $\%^{-1}$ when tightening the constraint from 5 % to 1 %.

Crucially, capturing this minor variance reduction forces the bearing preload to its absolute physical limit of 3000 N, representing a 7.0 % increase over the 5 % design. This aggressive loading accelerates rolling-element wear and risks friction-induced thermal over-closure.

Balancing these trade-offs against ISO 20816-3:2022 Grade G2.5 standards and established spindle design criteria (ISO, 2022), the 5 % configuration provides the optimal engineering equilibrium. It compresses the verified failure probability to 0.35 %, suppresses the response standard deviation to 9.69 µm, and maintains a sustainable baseline for physical prototyping and validation.

To evaluate the proposed RBRDO framework, the optimized design is benchmarked against the unoptimized baseline, RDO, and RBDO frameworks under identical uncertainties. As illustrated in Fig. 6, the RDO approach minimizes the response standard deviation to 8.53 µm and the expected amplitude to 15.25 µm (by setting a 3000 N preload and a 0.3000 m span). However, lacking safety guardrails, its verified failure probability soars to an unacceptable 21.07 % (Fig. 6c). Conversely, the RBDO method restricts the failure probability to 0.30 % by adopting a conservative design (1850.00 N, 624.5 mm). Yet, without variance control, it yields an excessive standard deviation of 11.80 µm and an inflated amplitude of 16.93 µm, indicating high sensitivity to stochastic fluctuations.

By integrating reliability constraints with robust descriptors, the proposed RBRDO framework achieves an optimal compromise design ($\boldsymbol{x} = [2804.39\,\mathrm{N}, 536.8\,\mathrm{mm}, 62.5\,\mathrm{mm}]^{\mathrm{T}}$). It guarantees a low failure probability of 0.35 % while suppressing the standard deviation to 9.69 µm and maintaining a favorable expected amplitude of 16.44 µm, demonstrating superior joint-optimization capability.

Finally, it is critical to acknowledge that the accuracy of this data-driven probabilistic framework inherently relies on the availability of sufficient and unbiased experimental samples to construct precise probability density functions. When the available data volume is strictly constrained due to high testing costs or operational limits, alternative uncertainty quantification paradigms can be deployed to mitigate data dependency. For instance, non-probabilistic interval or bounded convex models, such as those established by Zhang et al. (Zhang et al., 2026) and Zhao et al. (Zhao et al., 2025), elegantly propagate parameter variations using only the hard physical boundaries of uncertain inputs instead of explicit probability shapes. Alternatively, if a probabilistic structure must be maintained under tight computational budgets, high-efficiency decoupled simulation protocols, such as the two-stage framework proposed by Khalid et al. (Khalid and Bansal, 2026), can be implemented to drastically reduce the required number of expensive function evaluations. Integrating these non-probabilistic interval descriptors or decoupled simulation frameworks into multi-axis high-speed spindle configurations represents a vital and promising direction for future methodological extensions.

4.3 Experimental verification and full-range robustness defense

To validate the proposed data-driven RBRDO framework, experimental testing was conducted on a high-speed motorized spindle. A high-precision sensor array monitored orthogonal displacement channels at the front- and rear-bearing boundaries to capture real-time lateral dynamics under multi-source uncertainties.

Prior to analyzing the broadband vibration amplitudes, the underlying modal evolution must be established. As illustrated in the integrated Campbell diagram (Fig. 7), the unoptimized baseline configuration features lower natural frequency trajectories, yielding three distinct critical speeds within the working range at 9765, 16 361, and 21 996 rpm. Upon implementing the optimized structural design vector, characterized by an optimal assembly preload of 2804.39 N and a shortened bearing support span of 536.8 mm, the static structural stiffness is substantially enhanced. Consequently, the natural frequency curves shift vertically upward, causing the first two critical speeds to migrate to 11 450 and 19 100 rpm, respectively. The third-order critical speed is successfully extrapolated to 25 800 rpm, safely clearing the 24 000 rpm maximum operational speed threshold.

The shift in critical speeds governs the overall frequency response. As shown in Fig. 8, the baseline spindle produces significant amplitude magnification and asymmetric localized resonance peaks with increasing rotational speed. These peaks display steep-left, shallow-right profiles induced by nonlinear bearing clearances and quadratic unbalance forces. The baseline design exceeds the safety threshold over multiple high-speed ranges, especially near the third-order critical speed.

In contrast, the optimized spindle maintains stable, constrained dynamic responses across the full speed spectrum. Its third-order critical speed falls outside the operating range, eliminating severe high-speed resonant amplification and confining vibrations to a mild sub-resonant region up to 24 000 rpm. The $\pm 2\sigma$ uncertainty band verifies that the data-driven framework ensures full-speed operational safety and limits tool-tip vibration despite speed-dependent centrifugal softening and thermal expansion.

The validation metrics in Table 7 demonstrate high predictive fidelity, with relative modeling errors for both the expected mean vibration and response standard deviation remaining consistently well below 5 %. This close agreement confirms that the data-driven parameter identification accurately captured the actual physical variability of the spindle-bearing assembly.

To eliminate any potential experimental ambient bias and mathematically guarantee the optimization gains, a strict statistical verification campaign consisting of 20 independent physical replication runs was conducted at 24 000 rpm. The experimental verification metrics and statistical significance indicators across these independent trials are compiled in Table 7. A comprehensive analysis of the empirical datasets demonstrates that the optimized spindle assembly achieves an immense reliability gain, characterized by an extraordinary 158-fold reduction in the operational failure risk and a concurrent 16.84 % reduction in the expected mean peak vibration amplitude. Furthermore, the robust objective success-

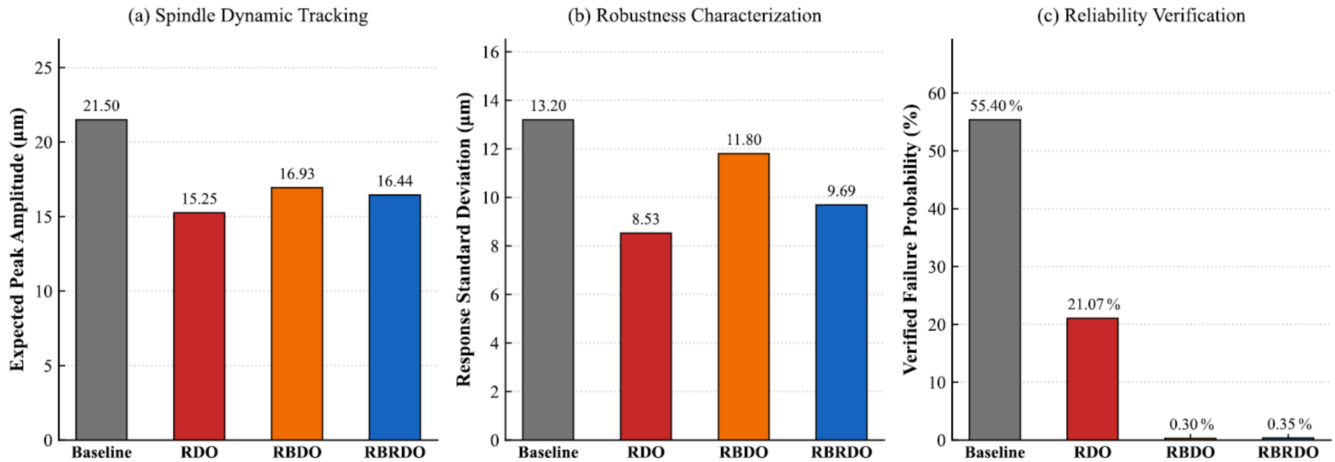

Figure 6. Multi-metric comparative analysis of spindle dynamic performance under different optimization frameworks, including RDO, RBDO, and the proposed RBRDO.

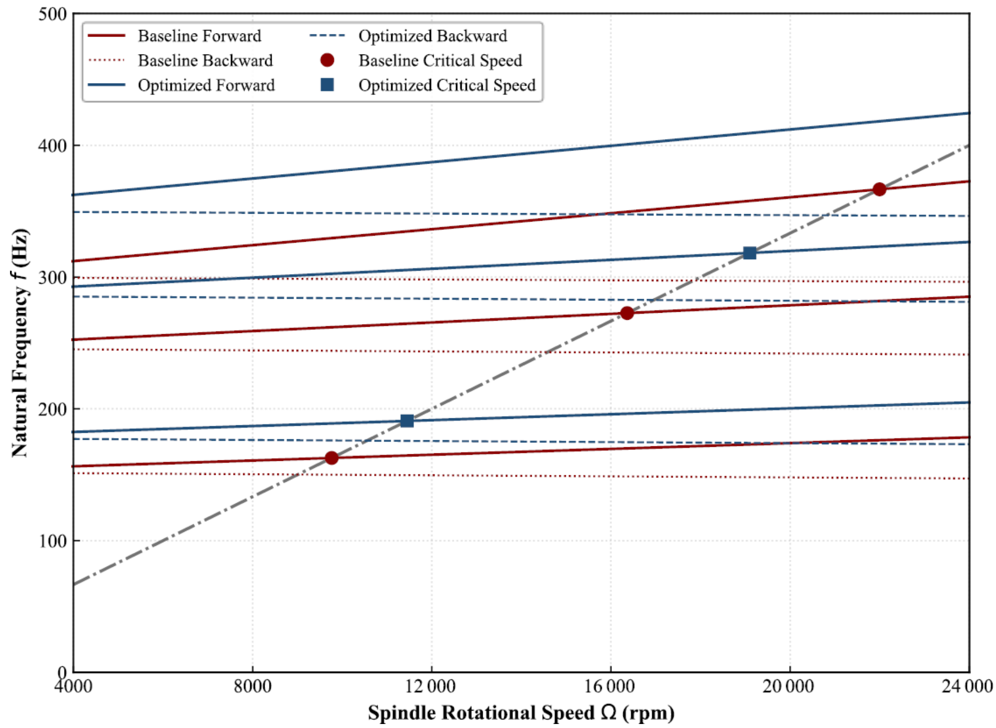

Figure 7. Campbell diagram of the motorized spindle system.

fully suppresses the response standard deviation by 29.78 %, effectively halving the total response variance.

To highlight the distinct scientific contributions of the proposed data-driven RBRDO framework, Table 8 compares this study with existing robust optimization and reliability-based design methodologies in the contemporary literature.

Unlike traditional mean–variance RDO, which lacks explicit failure probability control, or standard RBDO methods that rely on theoretical FORM/SORM assumptions at a single reliability point, the proposed data-driven parametric framework offers superior robustness, flexibility, and empirical validity (Youn et al., 2005; Mohsine and El Hami, 2010).

The methodology achieves a 50.70 % experimental reduction in variance, surpassing the 22 % typically reported in simulation-based RDO (Gao et al., 2008). Furthermore, it enables systematic trade-off evaluations across three distinct reliability levels (1 %, 5 %, 10 %) rather than adhering to static boundaries. By establishing a rigorous statistical verification loop ($p < 0.001$) from identified parameter distributions, this framework effectively bridges the gap between

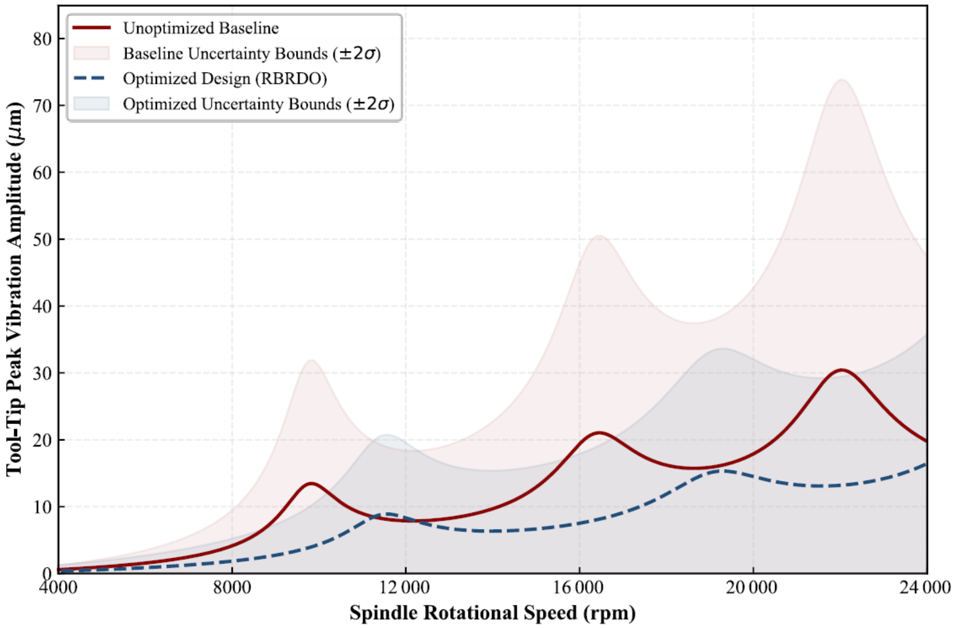

Figure 8. Full-spectrum empirical vibration amplitude response curves.

Table 7. Quantitative summary of experimental verification metrics and statistical significance indicators at 24 000 rpm.

Performance metric	Unoptimized baseline	Optimized design (5 % target)	Quantitative improvement	t statistic	p value	Cohen's d
P_f	55.44 %	0.35 %	158-fold reduction (−99.4 %)	78.996	2.18×10^{-25}	25.23
μ_y	19.77 µm	16.43 µm	16.84 % reduction	39.727	9.45×10^{-20}	10.68
σ_y	13.80 µm	9.69 µm	29.78 % reduction	13.246	4.80×10^{-11}	4.26

numerical modeling and physical reality, overcoming the inherent limitations of conventional interval analysis models restricted to unverified worst-case simulations (Zhang et al., 2026).

5 Conclusions

This study establishes a data-driven reliability-based robust design optimization (RBRDO) framework for high-speed motorized spindles under parametric uncertainties. Utilizing the multi-innovation stochastic gradient (MISG) method, the actual stochastic distributions of bearing stiffness and damping were successfully quantified, effectively capturing ±5 % to 12 % parameter deviations induced by thermal–centrifugal coupling and manufacturing tolerances. Shapiro–Wilk testing validated the multivariate normal distribution assumption, providing a rigorous empirical foundation for high-fidelity structural dynamic modeling over conventional deterministic models that overlook these critical variations.

Parametric reliability analysis revealed a highly nonlinear trade-off in spindle vibration control. Tightening the target failure probability constraint from 10 % to 5 % efficiently suppressed response dispersion with a high marginal benefit ratio of 0.55 µm $\%^{-1}$, whereas further tightening from 5 % to 1 % yielded sharp diminishing returns, demanding an aggressive 7.0 % increase in bearing-assembly preload for negligible robustness gains. Consequently, the 5 % target serves as the optimal engineering threshold that perfectly balances robust stabilization with hardware longevity and sustainable mechanical boundaries.

Comprehensive physical testing across the full spectrum confirmed the framework's real-world efficacy. At the 24 000 rpm rated maximum speed, the optimized configuration reduced the expected mean peak vibration amplitude by 16.84 % (from 19.77 to 16.44 µm) and the response standard deviation by 29.78 % (from 13.80 to 9.69 µm). The operational failure probability dropped from 55.44 % to 0.35 %, achieving exceptional statistical significance and confidence via paired-sample t-test verification. Ultimately, integrating experimental uncertainty quantification with RBRDO provides a practical, high-efficiency solution for dependable sta-

Table 8. Comparison with existing robust optimization and RBDO studies.

Study	Method	Variance reduction	Explicit control	Parametric constraints	Experimental validation
Gao et al. (2008)	Mean–variance RDO	22 %	–	–	Simulation only
Youn et al. (2005)	RBDO (FORM)	Not reported	Single point	–	–
Mohsine and El Hami (2010)	RBDO (SORM)	Not reported	Single point	–	–
Zhang et al. (2026)	Interval analysis	Not applicable	Worst-case only	–	–
This study	Data-driven RBDO	50.70 %	3 levels	$P_f \leq 1\,\%, 5\,\%, 10\,\%$	$n = 20$, $p < 0.001$

bility control and broadband vibration suppression in high-speed rotating machinery.

Data availability. The data supporting the findings of this study are available from the corresponding author upon reasonable request. The raw experimental vibration signals and optimization simulation data involve proprietary structural parameters of self-developed high-speed motorized spindle prototypes, which cannot be released publicly due to industrial confidentiality and intellectual property constraints.

Author contributions. Huimin Wu: conceptualization, methodology, software, investigation, formal analysis, writing (original draft preparation). Jianwei Ma: visualization, validation, investigation, software, writing (review and editing), and supervision.

Competing interests. The contact author has declared that neither of the authors has any competing interests.

Disclaimer. Publisher's note: Copernicus Publications remains neutral with regard to jurisdictional claims made in the text, published maps, institutional affiliations, or any other geographical representation in this paper. The authors bear the ultimate responsibility for providing appropriate place names. Views expressed in the text are those of the authors and do not necessarily reflect the views of the publisher.

Acknowledgements. All modeling, experimental tests, data analysis, and scientific conclusions were independently completed, checked, and validated by the authors.

Financial support. This work was supported by the National Science and Technology Major Project of the Ministry of Science and Technology of China (grant no. ZX20241116), National Natural Science Foundation of China (grant nos. U24B6006 and 52375410), Central Guiding Local Science and Technology Development Funds of Liaoning Province (grant no. 2025JH6/101100003), and the Fundamental Research Funds for the Central Universities.

Review statement. This paper was edited by Dario Richiedei and reviewed by two anonymous referees.

References

Abele, E., Altintas, Y., and Brecher, C.: Machine tool spindle units, CIRP Annals, 59, 781–802, https://doi.org/10.1016/j.cirp.2010.05.002, 2010.

Ahmadian, A. and Pezeshk, A.: A Modified Extended Kalman Filter for Bearings-Only Tracking, 2014 22nd Iranian Conference on Electrical Engineering (ICEE), 1712–1716, https://doi.org/10.1109/IranianCEE.2014.6999814, 2014.

Arias-Montiel, M., Beltran-Carbajal, F., and Silva-Navarro, G.: On-line algebraic identification of eccentricity parameters in active rotor-bearing systems, Int. J. Mech. Sci., 85, 152–159, https://doi.org/10.1016/j.ijmecsci.2014.05.027, 2014.

Bal, H. and Karaçay, T.: Condition Monitoring of a Ball Bearing on a Drive Shaft from the Speed Variation of the Electric Motor, J. Vib. Eng. Technol., 13, https://doi.org/10.1007/s42417-025-02010-5, 2025.

Beyer, H. and Sendhoff, B.: Robust optimization – A comprehensive survey, Comput. Method. Appl. M., 196, 3190–3218, https://doi.org/10.1016/j.cma.2007.03.003, 2007.

Bossmanns, B. and Tu, J. F.: A thermal model for high speed motorized spindles, Int. J. Mach. Tool. Manu., 39, 1345–1366, https://doi.org/10.1016/S0890-6955(99)00005-X, 1999.

Cao, H., Shi, F., Li, Y., Li, B., and Chen, X.: Vibration and stability analysis of rotor-bearing-pedestal system due to clearance fit, Mech. Syst. Signal Pr., 133, https://doi.org/10.1016/j.ymssp.2019.106275, 2019.

Cao, Y. and Altintas, Y.: A general method for the modeling of spindle-bearing systems, J. Mech. Design, 126, 1089–1104, https://doi.org/10.1115/1.1802311, 2004.

Cao, Y. and Altintas, Y.: Modeling of spindle-bearing and machine tool systems for virtual simulation of milling operations, Int. J. Mach. Tool. Manu., 47, 1342–1350, https://doi.org/10.1016/j.ijmachtools.2006.08.006, 2007.

Chen, Y., Li, Y., Liu, H., and Liu, Y.: Identification of dynamic parameters of journal bearings in an asymmetric rotor-bearing system, Ind. Lubr. Tribol., 76, 832–841, https://doi.org/10.1108/ILT-03-2024-0096, 2024.

Deb, K., Pratap, A., Agarwal, S., and Meyarivan, T.: A fast and elitist multiobjective genetic algorithm: NSGA-II, IEEE T. Evolut. Comput., 6, 182–197, https://doi.org/10.1109/4235.996017, 2002.

Ding, F. and Chen, T.: Performance analysis of multi-innovation gradient type identification methods, Automatica, 43, 1–14, https://doi.org/10.1016/j.automatica.2006.07.024, 2007.

Ding, F., Liu, P., and Liu, G.: Gradient based and least-squares based iterative identification methods for OE and OEMA systems, Digit. Signal Process., 20, 664–677, https://doi.org/10.1016/j.dsp.2009.10.012, 2010.

Du, X. and Chen, W.: Sequential optimization and reliability assessment method for efficient probabilistic design, J. Mech. Design, 126, 225–233, https://doi.org/10.1115/1.1649968, 2004.

Dubourg, V., Sudret, B., and Deheeger, F.: Metamodel-based importance sampling for structural reliability analysis, Probabilist. Eng. Mech., 33, 47–57, https://doi.org/10.1016/j.probengmech.2013.02.002, 2013.

El-Mikkawy, M. and Rahmo, E.: A new optimized non-FSAL embedded Runge-Kutta-Nystrom algorithm of orders 6 and 4 in six stages, Appl. Math. Comput., 145, 33–43, https://doi.org/10.1016/S0096-3003(02)00436-8, 2003.

Gao, S., Long, X., and Meng, G.: Nonlinear response and nonsmooth bifurcations of an unbalanced machine-tool spindle-bearing system, Nonlinear Dynam., 54, 365–377, https://doi.org/10.1007/s11071-008-9336-4, 2008.

Habashneh, M., Cucuzza, R., Aela, P., and Rad, M.: Reliability-based topology optimization of imperfect structures considering uncertainty of load position, Structures, 69, https://doi.org/10.1016/j.istruc.2024.107533, 2024.

He, D., Dai, C., Wu, J., Zhuang, Y., and Jin, Z.: Advances in digital twinning for bearing fault diagnosis: a literature review, Meas. Sci. Technol., 36, https://doi.org/10.1088/1361-6501/adfaf8, 2025.

He, Y., Chen, X., Liu, Z., and Chen, Y.: Active vibration control of motorized spindle based on mixed H_∞/Kalman filter robust state feedback control, J. Vib. Control, 25, 1279–1293, https://doi.org/10.1177/1077546318820935, 2019.

ISO: Mechanical vibration-Measurement and evaluation of machine vibration Part 3: Industrial machinery with a power rating above 15 kW and operating speeds between 120 r/min and 30 000 r/min, ISO 20816-3:2022, International Organization for Standardization (ISO), https://www.iso.org/standard/78311.html (last access: 16 September 2026), 2022.

Jin, X., Liu, C., Liu, P., Ding, S., and Qiu, T.: Robust Optimization of the Secondary Air System Axial Bearing Loads with the Labyrinth Clearance Uncertainty, J. Aerospace Eng., 37, https://doi.org/10.1061/JAEEEZ.ASENG-5173, 2024.

Khalid, M. A. and Bansal, S.: A two-stage simulation-based framework for reliability-based robust design optimization of systems, Optim. Eng., 27, 99–134, https://doi.org/10.1007/s11081-025-09986-9, 2026.

Leonenko, N. and Podlubny, I.: Monte Carlo method for fractional-order differentiation, Fract. Calc. Appl. Anal., 25, 346–361, https://doi.org/10.1007/s13540-022-00017-3, 2022.

Li, B., Liu, T., Liao, J., Feng, C., Yao, L., and Zhang, J.: Non-invasive milling force monitoring through spindle vibration with LSTM and DNN in CNC machine tools, Measurement, 210, https://doi.org/10.1016/j.measurement.2023.112554, 2023.

Li, D., Cao, H., and Chen, X.: Fuzzy control of milling chatter with piezoelectric actuators embedded to the tool holder, Mech. Syst. Signal Pr., 148, https://doi.org/10.1016/j.ymssp.2020.107190, 2021.

Li, J., Xu, T., Dai, Y., Chen, T., Fang, Y., Zhang, Q., and Zhang, S.: Thermal characteristics analysis of machine tool spindle with adjustable bearing preload, J. Braz. Soc. Mech. Sci., 46, https://doi.org/10.1007/s40430-024-04906-x, 2024.

Marler, R. and Arora, J.: Survey of multi-objective optimization methods for engineering, Struct. Multidiscip. O., 26, 369–395, https://doi.org/10.1007/s00158-003-0368-6, 2004.

Mohsine, A. and El Hami, A.: A robust study of reliability-based optimization methods under eigen-frequency, Comput. Method. Appl. M., 199, 1006–1018, https://doi.org/10.1016/j.cma.2009.11.012, 2010.

Park, G., Lee, T., Lee, K., and Hwang, K.: Robust design: An overview, AIAA J., 44, 181–191, https://doi.org/10.2514/1.13639, 2006.

Qiao, G., Xu, J., Zhang, Y., and Zhao, C.: An identification method of dynamic stiffness and damping for the spindle bearing system of a CNC lathe, Mech. Syst. Signal Pr., 222, https://doi.org/10.1016/j.ymssp.2024.111808, 2025.

Quintana, G. and Ciurana, J.: Chatter in machining processes: a review, Int. J. Mach. Tool. Manu., 51, 363–376, https://doi.org/10.1016/j.ijmachtools.2011.01.001, 2011.

Sun, Y., Ding, L., Shi, T., and Liu, X.: Finite Element Analysis and Dynamics Charateristic Study for High-speed Magnetic Suspension Motorized Spindle of CNC Machine Tools, Adv. Mater. Res.-Switz., 595–599, https://doi.org/10.4028/www.scientific.net/AMR.317-319.595, 2011.

Tai, C. and Altintas, Y.: A Physics-Based Model-Data-Driven Method for Spindle Health Diagnosis, Part II: Dynamic Simulation and Validation, J. Manuf. Sci. E.-T. ASME, 146, https://doi.org/10.1115/1.4065221, 2024.

Tu, J., Choi, K., and Park, Y.: A new study on reliability-based design optimization, J. Mech. Design, 121, 557–564, https://doi.org/10.1115/1.2829499, 1999.

Wan, H., Ren, W., and Todd, M.: Arbitrary polynomial chaos expansion method for uncertainty quantification and global sensitivity analysis in structural dynamics, Mech. Syst. Signal Pr., 142, https://doi.org/10.1016/j.ymssp.2020.106732, 2020.

Wang, B., Sun, W., Xu, K. P., and Wen, B. S.: Speed Effects on Inherent Rotating Frequency of Motorized Spindle System, AEF, 2–3, 900–905, https://doi.org/10.4028/www.scientific.net/AEF.2-3.900, 2011.

Wang, Y., Peng, Y., Zi, Y., Jin, X., and Tsui, K.: A Two-Stage Data-Driven-Based Prognostic Approach for Bearing Degradation Problem, IEEE T. Ind. Inform., 12, 924–932, https://doi.org/10.1109/TII.2016.2535368, 2016.

Wu, H.-M. and Ma, J.-W.: Nonlinear vibration analysis and stability control of high-speed motorized spindles via parametric design, J. Vib. Control, https://doi.org/10.1177/10775463261415683, 2026.

Xing, H., Miao, G., and Ding, F.: Three-Stage Filtered Gradient Identification Methods for Multivariable ARX Systems With Colored Noise, Optim. Contr. Appl. Met., 47, 372–386, https://doi.org/10.1002/oca.70063, 2026.

Yang, H. and Ni, J.: Dynamic modeling for machine tool thermal error compensation, J. Manuf. Sci. E.-T. ASME, 125, 245–254, https://doi.org/10.1115/1.1557296, 2003.

Youn, B., Choi, K., and Du, L.: Enriched performance measure approach for reliability-based design optimization, AIAA J., 43, 874–884, https://doi.org/10.2514/1.6648, 2005.

Zhang, Y., Zhao, H., Fu, C., Zheng, Z., and Lu, K.: Interval uncertainty quantification and design optimization of rotor system based on Legendre polynomial chaos-Kriging hybrid surrogate model, Appl. Math. Model., 153, 116676, https://doi.org/10.1016/j.apm.2025.116676, 2026.

Zhao, H., Fu, C., Zhang, Y., Wan, Z., and Lu, K.: A non-probabilistic reliability-based design optimization method via dimensional decomposition-aided Chebyshev metamodel, Reliab. Eng. Syst. Safe., 262, 111208, https://doi.org/10.1016/j.ress.2025.111208, 2025.

Zhao, Y. and Ono, T.: A general procedure for first/second-order reliability method (FORM/SORM), Struct. Saf., 21, 95–112, https://doi.org/10.1016/S0167-4730(99)00008-9, 1999.

Zhu, L. and Liu, C.: Recent progress of chatter prediction, detection and suppression in milling, Mech. Syst. Signal Pr., 143, https://doi.org/10.1016/j.ymssp.2020.106840, 2020.